Achieving Centimeter Accuracy Indoor Localization on WiFi Platforms: A Frequency Hopping Approach

Chen Chen, *Student Member, IEEE,* Yan Chen, *Senior Member, IEEE,* Yi Han, *Student Member, IEEE,* Hung-Quoc Lai, and K. J. Ray Liu, *Fellow, IEEE*

***Abstract*—Indoor positioning systems are attracting more and more attention from the academia and industry recently. Among them, approaches based on WiFi techniques are more favorable since they are built upon the WiFi infrastructures available in most indoor spaces. However, due to the bandwidth limit in mainstream WiFi systems, the indoor positioning system leveraging WiFi techniques can hardly achieve centimeter localization accuracy under strong non-line-of-sight conditions, which is common for indoor spaces. In this paper, we present a WiFi-based indoor positioning system that achieves centimeter accuracy in non-line-of-sight scenarios by exploiting the frequency diversity via frequency hopping. During the offline phase, the system collects channel state information from multiple channels at locations-of-interest. Then, the channel state information are post-processed to combat the synchronization errors and interference. The channel state information from multiple channels are then combined into location fingerprints via bandwidth concatenation and in a database. During the online phase, channel state information from an unknown location are formulated into the location fingerprint and is compared against the fingerprints in the database using the time-reversal resonating strength. Finally, the location is determined by the calculated time-reversal resonating strengths. Extensive experiment results demonstrate a perfect centimeter accuracy in an office environment in non-line-of-sight scenarios with only one pair of single-antenna WiFi devices.**

***Index Terms*—WiFi, indoor localization, channel state information, time-reversal, resonating strength.**

I. Introduction

Global Positioning System (GPS) is an outdoor positioning system that provides real-time location information under all weather conditions near the Earth's surface, as long as there exists an unobstructed line-of-sight (LOS) from the device to at least four GPS satellites [1]. On the other hand, accurate indoor localization is highly desirable, since nowadays people spend much more time indoor than outdoor. A high accuracy indoor positioning system (IPS) can enable a wide variety of applications, e.g., providing museum guides to tourists by localizing their exact locations [2], or supplementing users with location information in shopping malls [3]. Unfortunately, the GPS signal cannot provide reliable location information indoor, since it is severely attenuated by the walls in the building and scattered by numerous reflectors in an indoor environment.

All the authors are with Origin Wireless, Inc., Greenbelt, MD 20770 USA. Chen Chen, Yi Han, and K. J. Ray Liu are also with the Department of Electrical and Engineering, University of Maryland College Park, College Park, MD 20742 USA (e-mail: {cc8834, yhan1990, kjrliu}@umd.edu). Yan Chen is also with University of Electronic Science and Technology of China, Chengdu, Sichuan, China (e-mail: eecyan@uestc.edu.cn). Hung-Quoc Lai is with Origin Wireless Inc. (e-mail: quoc.lai@originwireless.net).

Many research efforts have been devoted to the development of accurate and robust IPSs. According to the technologies adopted, these IPSs can be further classified into two classes, i.e., ranging-based and fingerprint-based [4]. For the ranging-based methods, at least three anchors are deployed into the indoor environment to triangulate the device through measuring the relative distances between the device to the anchors. The distances are generally obtained from other measurements, e.g., received signal strength indicator (RSSI) and time of arrival (TOA). RSSI-based ranging methods [5]–[7] utilizes the path-loss model to derive the distance and can typically achieve an accuracy of $1 \sim 3$m on average under LOS scenarios, while TOA-based ranging methods retrieve the TOA of the first arrived multipath component from the channel impulse response (CIR). To achieve a fine timing resolution, TOA-based methods require a large bandwidth, which is available with ultra-wideband (UWB) techniques. With UWB, the localization accuracy is $10 \sim 15$cm in a LOS setting [8], [9].

On the other hand, the fingerprint-based approaches harness the naturally existing spatial features associated with different locations, e.g., RSSI, CIR, and channel state information (CSI), where CSI is a fine-grained information readily available in WiFi systems that portraits the environment. In these schemes, fingerprints of different locations are stored in a database during the offline phase. In the online phase, the fingerprint of the current location is compared against those in the database to estimate the device location. In [10]–[12], RSSI values from multiple access points (APs) are utilized as the fingerprint, leading to an accuracy of $2 \sim 5$m. The accuracy is further improved to $0.95 \sim 1.1$m by taking CSIs as the fingerprint [13]–[15]. In [16], Zhung-Han *et al.* obtain CIR fingerprints under a bandwidth of 125 MHz and calculate the time-reversal (TR) resonating strength as the similarity measure among different locations, which gives an accuracy of $1 \sim 2$cm under non-line-of-sight (NLOS) scenarios.

Summarizing the ranging-based and fingerprint-based schemes, we find that

1) *The accuracy of the ranging-based methods are susceptible to the correctness of the physical rules, e.g., path-loss model, which degrades severely in the complex indoor environment.* The existence of large number of multipath components and blockage of obstacles in indoor spaces impair the precision of the physical rules.
2) *The fingerprint-based methods, which can work under strong NLOS environment, require a large bandwidth for accurate localization.* Since the maximum bandwidth of

the mainstream 802.11n is 40 MHz, IPSs utilizing WiFi techniques cannot resolve enough independent multipath components in the environment. The shortage of available bandwidth introduces ambiguities into fingerprints associated with different locations, and thus degrades the localization accuracy. On the other hand, a bandwidth as large as 125 MHz that leads to centimeter accuracy [16] can only be achieved on dedicated hardware and incurs additional costs in deployment.

Is there any approach that can achieve the centimeter localization accuracy using WiFi devices in an NLOS environment? The answer is affirmative. In [17], Chen *et al.* present an IPS that achieves centimeter accuracy using one pair of single-antenna WiFi devices under strong NLOS conditions using frequency hopping. The IPS obtains CSIs and formulates location fingerprints from multiple WiFi channels in the offline phase, and calculates TR resonating strengths for localization in the online phase. However, interference from other WiFi networks might corrupt the fingerprint, which is neglected in [17]. To deal with the interference, in this work, we introduce an additional step of CSI sifting. Moreover, we utilize CSI averaging to mitigate the impact of channel noise and refine the fingerprint. Additionally, we provide much more details and analysis on the experiment results. In comparison with the existing works, the proposed method embraces the multipath effect and is infrastructure-free since it is built upon the WiFi networks available in most indoor spaces.

The main contributions of this work can be summarized as follows:

- We propose an IPS that can achieve centimeter accuracy in an NLOS environment with one pair of single-antenna WiFi devices. The proposed IPS eliminates the impact of interference from other WiFi networks through the process of CSI sifting.
- Leveraging the frequency diversity, we demonstrate that a large effective bandwidth can be achieved on WiFi devices by means of frequency hopping to overcome the issue of location ambiguity issue on traditional WiFi-based approaches.
- We conduct extensive experiments in a typical office environment to show the centimeter accuracy within an area of 20cm$\times$70cm under strong NLOS conditions.

The rest of the paper is organized as follows. In Section II, we introduce the TR technique and the channel estimation in WiFi systems. In Section III, we elaborate on the proposed localization algorithm. In Section IV, we present the experiment results in a typical office environment. Finally, we draw conclusions in Section V.

II. Preliminaries

In this part, we introduce the background of the TR technique and the channel estimation schemes in WiFi systems.

A. Time-Reversal

TR is a signal processing technique capable of mitigating the phase distortion of a signal passing a linear time-invariant (LTI) filtering system. It is based upon the fact that when the LTI system $h(t)$ is concatenated with its time-reversed and conjugated version $h^*(-t)$, the phase distortion is completely cancelled out at a particular time instance.

A physical medium can be regarded as LTI if it satisfies inhomogeneity and invertibility. When both conditions hold, TR focuses the signal energy at a specific time and at a particular location, known as the spatial-temporal focusing effect. Such focusing effect is observed experimentally in the field of ultrasonics, acoustics, as well as electromagnetism [18]–[21]. Leveraging the focusing effect, TR is applied successfully to the broadband wireless communication systems [22].

Fig. 1 shows the architecture of the TR communication system consisting of two phases, namely, channel probing phase and transmission phase. Here, we assume that transceiver A intends to send some data to transceiver B. During the channel probing phase, transceiver B sends an impulse signal to transceiver A, and transceiver A extracts the CIR based on the impulse signal, time-reverses, and takes conjugate of the CIR to generate a waveform. During the transmission phase, transceiver A convolves the transmitted signal with the waveform and sends to transceiver B. In this process, the channel acts as a natural matched filter due to the time-reversal operation. The TR focusing effect could be observed at a specific time instance and only at the exact location of transceiver B.

In virtue of the high-resolution TR focusing effect, in this work, we utilize TR as the signal processing technique to measure the similarity among fingerprints of different locations.

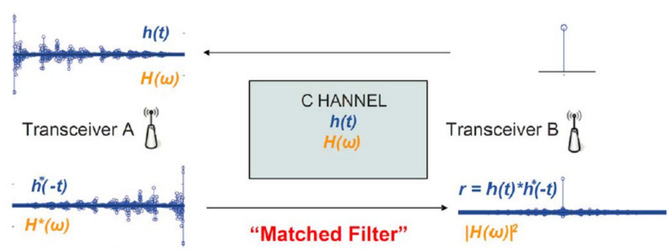

Fig. 1. The architecture of TR wireless communication system.

B. Channel Estimation in WiFi systems

In a WiFi system adopting the orthogonal frequency-division multiplexing (OFDM), the transmitted data symbols are spread onto several subcarriers to improve the robustness of the wireless communication against frequency-selective fading. Assuming a total of K usable subcarriers and denote the transmitted data symbol on the k-th subcarrier with index u_k as X_{u_k}, the received signal on subcarrier u_k, denoted by Y_{u_k}, takes the form as [23]

$$Y_{u_k} = H_{u_k} X_{u_k} + W_{u_k},\ k = 1, 2, \cdots, K, \tag{1}$$

where H_{u_k} is the CSI on subcarrier u_k and W_{u_k} is the complex Gaussian noise on subcarrier u_k.

To facilitate channel estimation, two identical sequences consisting of predetermined data symbols, known as the long

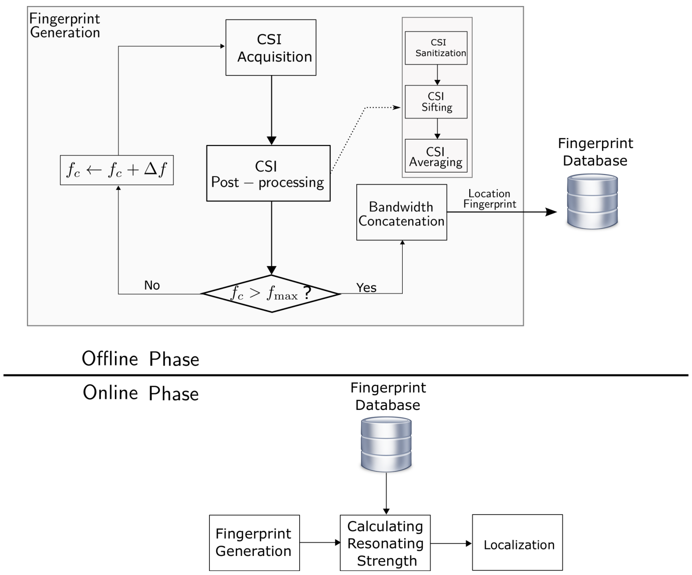

Fig. 2. Flowchart of the algorithm.

training preamble (LTP), are appended before the actual data frames. Therefore, given known LTP data symbols $X_{u_k,0}$, the CSI H_{u_k} can be estimated by [24]

$$\hat{H}_{u_k} = \frac{Y_{u_k}}{X_{u_k,0}},\ k = 1, 2, \cdots, K. \tag{2}$$

Eq. (2) is only valid in the absence of synchronization errors. In practice, synchronization errors cannot be neglected and they introduce additional phase rotations into $\hat{H}_{u_k}$. The synchronization errors are mainly composed by (i) channel frequency offset (CFO) ϵ caused by the misalignment of the local oscillators at the WiFi transmitter and receiver (ii) sampling frequency offset (SFO) η due to the mismatch between the sampling clock frequencies at the WiFi transmitter and receiver (iii) symbol timing offset (STO) Δn_0 caused by the imperfect timing synchronization at the WiFi receiver.

In the presence of the aforementioned synchronization errors, the CSI associated with the i-th LTP, denoted as $\hat{H}_i^{u_k}$, can be rewritten as [25]

$$\hat{H}_i^{u_k} = H_{u_k} e^{j2\pi(\beta_i u_k + \alpha_i)} + W_{i,u_k},\ k = 1, 2 \cdots, K\ , \tag{3}$$

where

$$\alpha_i = \left(\frac{1}{2} + \frac{iN_s + N_g}{N}\right)\epsilon \tag{4}$$

$$\beta_i = \frac{\Delta n_0}{N} + \left(\frac{1}{2} + \frac{iN_s + N_g}{N}\right)\eta \tag{5}$$

are the initial and linear phase distortions respectively. N is the size of Fast Fourier Transform (FFT), N_g is the length of the cyclic prefix, N_s is the total length of one OFDM frame with length $N + N_g$, and W_{i,u_k} is the estimation noise on subcarrier u_k for the i-th LTP, which can be modeled as complex Gaussian noise [26].

III. Proposed Algorithm

A. Calculation of the TR Resonating Strength in Frequency Domain

In the proposed IPS, the similarity of locations are measured by the TR resonating strength between their fingerprints. In this section, we provide details of TR resonating strength computation.

Given two time-domain CIRs $\hat{\mathbf{h}}$ and $\hat{\mathbf{h}}'$, with $\hat{\mathbf{h}} = [\hat{h}[0], \hat{h}[1], \cdots, \hat{h}[L-1]]^T$ and $\hat{\mathbf{h}}'$ defined similarly, where T is the transpose operator, the resonating strength between $\hat{\mathbf{h}}$ and $\hat{\mathbf{h}}'$ is calculated as [16]

$$\gamma_{\mathsf{CIR}}[\hat{\mathbf{h}}, \hat{\mathbf{h}}'] = \frac{\max_i \left| \left(\hat{\mathbf{h}} * \hat{\mathbf{g}}\right)[i] \right|^2}{\langle \hat{\mathbf{h}}, \hat{\mathbf{h}} \rangle \langle \hat{\mathbf{g}}, \hat{\mathbf{g}} \rangle}\ , \tag{6}$$

where $*$ denotes the convolution operator, $\hat{\mathbf{g}}$ is the time-reversed and conjugate version of $\hat{\mathbf{h}}'$, and $\langle \mathbf{x}, \mathbf{y} \rangle$ is the inner product operator between vector $\mathbf{x}$ and vector $\mathbf{y}$, expressed by $\mathbf{x}^\dagger \mathbf{y}$. Here, $(\cdot)^\dagger$ is the Hermitian operator. Notice that, the computation of $\gamma_{\mathsf{CIR}}[\hat{\mathbf{h}}, \hat{\mathbf{h}}']$ removes the impact of STO by searching all possible index i across the output of $\left|\left(\hat{\mathbf{h}} * \hat{\mathbf{h}}'\right)[i]\right|$. It can be shown that $0 \le \gamma_{\mathsf{CIR}}[\hat{\mathbf{h}}, \hat{\mathbf{h}}'] \le 1$.

Since the convolution in time domain is equivalent to the inner product in frequency domain [27], the TR resonating strength can be calculated using CSIs, the frequency-domain counterparts of CIRs. Given two CSIs $\hat{\mathbf{H}} = [\hat{H}_{u_1}, \hat{H}_{u_2}, \cdots, \hat{H}_{u_K}]^T$ and $\hat{\mathbf{H}}'$ defined similarly, and assume that the synchronization errors are mostly mitigated, the TR resonating strength in frequency domain is given by

$$\gamma[\hat{\mathbf{H}}, \hat{\mathbf{H}}'] = \frac{\left|\sum_{k=1}^{K} \hat{H}_{u_k} \hat{H}'_{u_k}\right|^2}{\langle \hat{\mathbf{H}}, \hat{\mathbf{H}} \rangle \langle \hat{\mathbf{H}}', \hat{\mathbf{H}}' \rangle}\ . \tag{7}$$

It is straightforward to prove that $0 \le \gamma[\hat{\mathbf{H}}, \hat{\mathbf{H}}'] \le 1$, and $\gamma[\hat{\mathbf{H}}, \hat{\mathbf{H}}'] = 1$ if and only if $\hat{\mathbf{H}} = C\hat{\mathbf{H}}'$ where $C \neq 0$ is any complex scaling factor. Therefore, the TR resonating strength can be regarded as a measure of similarity between two CSIs.

B. Indoor Localization Based on TR Resonating Strength

The proposed localization algorithm consists of an offline phase and an online phase. The details of the two phases are illustrated in Fig. 2 and are elaborated below.

1) Offline Phase: In the offline phase, the CSIs are measured at D channels, denoted by $f_1, f_2, \cdots, f_d, \cdots, f_D$, and at L locations-of-interest, denoted by $1, 2, \cdots, \ell, \cdots, L$. Assume that a total of N_{ℓ,f_d} CSIs are measured from the first and second LTPs at location ℓ and channel f_d, we write the CSI matrix as

$$\hat{\mathbb{H}}_i[\ell, f_d] = \left[\hat{\mathbf{H}}_{i,1}[\ell, f_d] \cdots \hat{\mathbf{H}}_{i,m}[\ell, f_d] \cdots \hat{\mathbf{H}}_{i,N_{\ell,f_d}}[\ell, f_d]\right], \tag{8}$$

where $m = 1, 2, \cdots, N_{\ell,f_d}$ is the realization index, $i \in \{1, 2\}$ is the LTP index, and $\hat{\mathbf{H}}_{i,m}[\ell, f_d] = [\hat{H}_{i,m}^{u_1}[\ell, f_d] \cdots \hat{H}_{i,m}^{u_k}[\ell, f_d] \cdots \hat{H}_{i,m}^{u_K}[\ell, f_d]]^T$ with $\hat{H}_{i,m}^{u_1}[\ell, f_d]$ standing for the m-th CSI of the i-th LTP on subcarrier u_k, and at location ℓ, channel f_d.

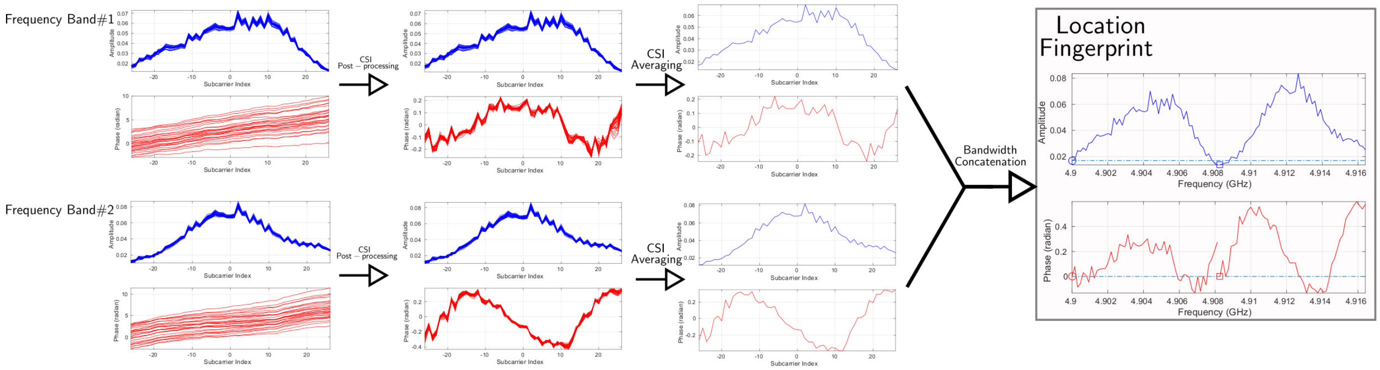

Fig. 3. An example of CSI post-processing, channel fingerprint generation, and location fingerprint generation.

The location fingerprint is generated from $\hat{\mathbb{H}}_i\left[\ell, f_d\right]$. The process contains 4 steps, which are presented below.

1. CSI Sanitization

The captured CSIs must be sanitized so as to mitigate the impact of initial and linear phase distortions shown in (3). First of all, we estimate the residual CFO and SFO from the channel estimation using [28]

$$\Omega_m^{u_k}[\ell, f_d] = \left[\hat{H}_{1,m}^{u_k}[\ell, f_d]\right]^* \times \hat{H}_{2,m}^{u_k}[\ell, f_d]$$
$$= e^{j2\pi\frac{N_s}{N}\phi_{u_k}}|H_{1,m}^{u_k}[\ell, f_d]|^2 \mathrm{sinc}^2\left(\pi\phi_{u_k}\right) + \psi_m^{u_k}[\ell, f_d], \quad (9)$$

where $\phi_k = \epsilon + \eta k$, $\mathrm{sinc}^2\left(\pi\phi_k\right) \approx 1$ since $\pi\phi_{u_k}$ is small, and $\psi_m^{u_k}[\ell, f_d]$ contains all cross terms. Therefore, ϕ_{u_k} can be estimated by

$$\hat{\phi}_{u_k} = \measuredangle\left[\Omega_m^{u_k}[\ell, f_d]\right], \quad (10)$$

where $\measuredangle[X]$ is the angle of X measured in radians. Compensating $\hat{\phi}_{u_k}$ gives

$$\tilde{H}_{i,m}^{u_k}[\ell, f_d] = \hat{H}_{i,m}^{u_k}[\ell, f_d]e^{-j\pi\hat{\phi}_{u_k}}e^{-j2\pi\frac{N_g+(i-1)N_s}{N}\hat{\phi}_{u_k}} \quad (11)$$

Substituting (11) into (8) and writing the updated $\hat{\mathbb{H}}_i\left[\ell, f_d\right]$ in (8) as $\tilde{\mathbb{H}}_i\left[\ell, f_d\right]$, we take the average of $\tilde{\mathbb{H}}_1\left[\ell, f_d\right]$ and $\tilde{\mathbb{H}}_2\left[\ell, f_d\right]$ as $\tilde{\mathbb{H}}\left[\ell, f_d\right] = \left(\tilde{\mathbb{H}}_1\left[\ell, f_d\right] + \tilde{\mathbb{H}}_2\left[\ell, f_d\right]\right)/2$.

After the removal of residual CFO and SFO, the STO still remains to be compensated. Write

$$\tilde{\mathbb{H}}\left[\ell, f_d\right] = \left[\tilde{\mathbf{H}}_1[\ell, f_d]\cdots\tilde{\mathbf{H}}_m[\ell, f_d]\cdots\tilde{\mathbf{H}}_{N_{\ell,f_d}}[\ell, f_d]\right], \quad (12)$$

where $\tilde{\mathbf{H}}_m[\ell, f_d] = [\tilde{H}_m^{u_1}[\ell, f_d]\cdots\tilde{H}_m^{u_k}[\ell, f_d]\cdots\tilde{H}_m^{u_K}[\ell, f_d]]^T$ is the CSI vector for the m-th realization on usable subcarriers after CFO/SFO correction. Denote $A_m^{u_k}[\ell, f_d] = \measuredangle\left\{\tilde{H}_m^{u_k}[\ell, f_d]\right\}$ as the angle of $\tilde{H}_m^{u_k}[\ell, f_d]$, we perform phase unwrapping on $A_m^{u_k}[\ell, f_d]$ to yield $A_m^{'u_k}[\ell, f_d]$. The slope of $A_m^{'u_k}[\ell, f_d]$ is linear with STO if we disregard the noise and interference. To estimate the slope, we perform a least-square fitting on $A_m^{'u_k}[\ell, f_d]$ expressed by

$$\widehat{\Delta n_0} = \frac{N\sum_{k=1}^K\left[(u_k - \overline{u})\right]\left[A_m^{'u_k}[\ell, f_d] - \overline{A}\right]}{2\pi\sum_{k=1}^K\left[u_k - \overline{u}\right]^2}, \quad (13)$$

where $\overline{u} = \frac{\sum_{k=1}^K u_k}{K}$ and $\overline{A} = \frac{\sum_{k=1}^K A_m^{'u_k}[\ell, f_d]}{K}$. Therefore, $\tilde{H}_m^{u_k}[\ell, f_d]$ is compensated as

$$\check{H}_m^{u_k}[\ell, f_d] = \tilde{H}_m^{u_k}[\ell, f_d]e^{-ju_k\widehat{\Delta n_0}\frac{2\pi}{N}}. \quad (14)$$

The compensated CSI matrix is denoted by

$$\check{\mathbb{H}}\left[\ell, f_d\right] = \left[\check{\mathbf{H}}_1[\ell, f_d]\cdots\check{\mathbf{H}}_m[\ell, f_d]\cdots\check{\mathbf{H}}_{N_{\ell,f_d}}[\ell, f_d]\right]. \quad (15)$$

2. CSI Sifting

Due to the presence of other WiFi devices in the environment, some CSI measurements might suffer from large interference from the traffic of nearby WiFi devices or radio-frequency systems, and should be excluded from further calculations. The interference introduces random noise onto the CSIs and impairs the CSI qualities. To combat the interference, firstly, we use $\check{\mathbf{H}}_m[\ell, f_d]$ to calculate the $N_{\ell,f_d} \times N_{\ell,f_d}$ resonating strength matrix $\mathbb{R}_{\ell,f_d}$, where $\check{\mathbf{H}}_m[\ell, f_d] = \left[\check{H}_m^{u_1}[\ell, f_d]\cdots\check{H}_m^{u_k}[\ell, f_d]\cdots\check{H}_m^{u_K}[\ell, f_d]\right]^T$ with $\gamma[\cdot,\cdot]$ defined in (7). The (i, j)-th entry of $\mathbb{R}_{\ell,f_d}$ is

$$\left[\mathbb{R}_{\ell,f_d}\right]_{i,j} = \gamma\left[\check{\mathbf{H}}_i[\ell, f_d], \check{\mathbf{H}}_j[\ell, f_d]\right]. \quad (16)$$

Secondly, we compute the column-wise average of $\mathbb{R}_{\ell,f_d}$ denoted as O_j with $j = 1, 2, \cdots, N_{\ell,f_d}$, given by

$$O_j = \frac{1}{N_{\ell,f_d} - 1}\sum_{\substack{i=1,2,\cdots,N_{\ell,f_d}\\ i\neq j}}\left[\mathbb{R}_{\ell,f_d}\right]_{i,j}. \quad (17)$$

Finally, we remove the j'-th column of $\check{\mathbb{H}}\left[\ell, f_d\right]$ if $O_{j'} \leq \tau$, where τ is a threshold.

We assume that the number of remaining CSIs after CSI sifting is N'_{ℓ,f_d}, and the corresponding index of the remaining CSIs are $t_1, \cdots, t_m, \cdots, t_{N'_{\ell,f_d}}$.

3. CSI Averaging

At location ℓ, for channel f_d, we generate the averaged CSI $\mathbf{S}\left[\ell, f_d\right] = [S_{\ell,f_d}^{u_1}\cdots S_{\ell,f_d}^{u_k}\cdots S_{\ell,f_d}^{u_K}]^T$ with dimension $K \times 1$ as

$$\mathbf{S}\left[\ell, f_d\right] = \frac{1}{N'_{\ell,f_d}}\sum_{m=1}^{N'_{\ell,f_d}}\check{\mathbf{H}}_{t_m}[\ell, f_d]\cdot\mathbf{W}_m, \quad (18)$$

where $\cdot$ stands for the element-wise dot product between two vectors. $\mathbf{W}_m$ is a $K \times 1$ vector represented as

$$\mathbf{W}_m = \begin{bmatrix} w_m[\ell, f_d] & w_m[\ell, f_d] & \cdots & w_m[\ell, f_d]\end{bmatrix}^T, \quad (19)$$

where $w_m[\ell, f_d] = e^{j\left(\measuredangle\left[\check{H}_{t_1}^{u_1}[\ell,f_d]\right]-\measuredangle\left[\check{H}_{t_m}^{u_1}[\ell,f_d]\right]\right)}$. The purpose of introducing $\mathbf{W}_m$ is to match the initial phases of $\check{\mathbf{H}}_{t_m}[\ell, f_d]$ with $m > 1$ to the first realization $\check{\mathbf{H}}_{t_1}[\ell, f_d]$, so that $\check{\mathbf{H}}_{t_m}[\ell, f_d]$ can be accumulated coherently, and the noise variance contained in $\check{\mathbf{H}}_{t_m}[\ell, f_d]$ is reduced by N'_{ℓ,f_d} times consequently.

4. Bandwidth Concatenation

At location ℓ, we obtain the fingerprint vector with dimension $DK \times 1$ by concatenating the averaged CSIs from all channels $\{f_d\}_{d=1,2,\cdots,D}$ as

$$\mathbf{G}[\ell] = \left[\mathbf{S}^T[\ell, f_1]\, V_1 \cdots \mathbf{S}^T[\ell, f_d]\, V_d \cdots \mathbf{S}^T[\ell, f_D]\, V_D\right]^T, \tag{20}$$

where $V_d = e^{-j\measuredangle\left[S_{\ell,f_d}^{u_1}\right]}$ is introduced to nullify the initial phases of different $\mathbf{S}^T[\ell, f_d]$.

Fig. 3 demonstrates an example of the fingerprint generation procedure. As can be observed from Fig. 3, the CSI post-processing effectively removes the phase distortions caused by the synchronization errors. The CSI averaging combines different realizations coherently, and the bandwidth concatenation associates two averaged CSI into the location fingerprint.

Since we concatenate all available bandwidths from D channels, we achieve a much larger effective bandwidth denoted by $W_e = DW$, where W is the bandwidth per channel.

2) Online Phase: The CSIs from an unknown location are formulated into the location fingerprint in the same manner as described in the offline phase. Assume that the location fingerprint from the unknown location ℓ' is given by $\mathbf{G}[\ell']$, the resonating strength between location ℓ' and location ℓ is computed as $\gamma[\mathbf{G}[\ell], \mathbf{G}[\ell']]$. Define $\ell^\star = \underset{\ell=1,2,\cdots,L}{\operatorname{argmax}}\ \gamma[\mathbf{G}[\ell], \mathbf{G}[\ell']]$, the estimated location $\hat{\ell}'$ takes the form

$$\hat{\ell}' = \begin{cases} \ell^\star, & \text{if } \gamma[\mathbf{G}[\ell^\star], \mathbf{G}[\ell']] \geq \Gamma \\ 0, & \text{Otherwise} \end{cases}, \tag{21}$$

where Γ is a tunable threshold. Notice that, in case of $\gamma[\mathbf{G}[\ell^\star], \mathbf{G}[\ell']] < \Gamma$, the proposed IPS fails to localize the device, and the algorithm returns 0 to imply an *unknown location*.

In Fig. 4, we show an example of location fingerprints generated at two different locations in different colors. For each location, we formulate 5 location fingerprints. As we can see, the differences among the location fingerprints at the same location are minor, while the differences of location fingerprints between the two different locations are much more pronounced.

IV. Experiment Results

A. Experiment Settings

Fig. 5 shows the setups of the experiments with details given below.

1) Environment: The experiments are conducted in a typical office suite composed by a large and a small office room in a multi-storey building. The two office rooms are blocked by a wall. In addition to the two large desks, the indoor space is filled with other furniture including chairs and computers, which are not shown in Fig. 5 for brevity.

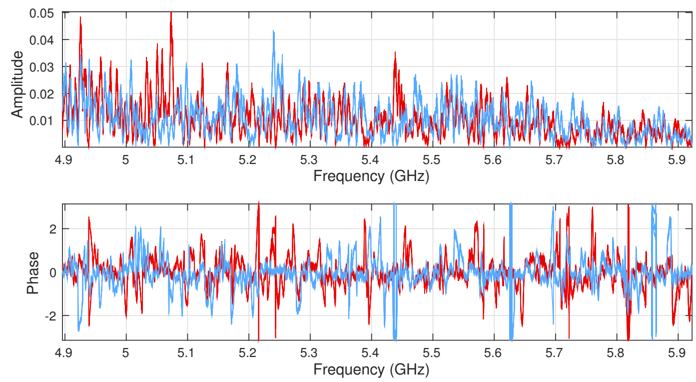

Fig. 4. A snapshot of location fingerprint after bandwidth concatenation generated at two different locations.

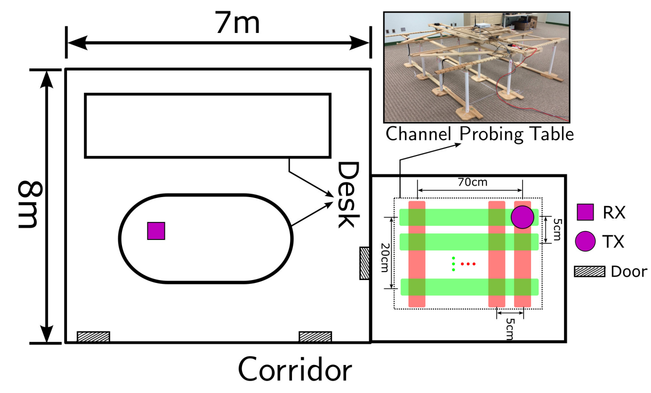

Fig. 5. Experiment settings.

2) Devices: Two Universal Software Radio Peripherals (USRPs) [29] are deployed as the WiFi transmitter and receiver respectively. For both devices, the bandwidth of each channel is configured as $W = 10$ MHz. The USRP transmitter sends WiFi signals compatible with 802.11a/g/p, while the USRP receiver performs timing and frequency synchronization, channel estimation, equalization, and data frame decoding. CSIs with correctly decoded data frames are recorded. The two USRPs perform frequency hopping to the next channel simultaneously after a sufficient number of CSIs are obtained on the current channel.

3) Details of Measurement: The WiFi transmitter is placed on a rectangular measurement structure in the small room. The WiFi receiver is placed on the table of the larger room.

The stepsize of the frequency hopping is configured as $W = 10$ MHz. We measure the frequency band from 4.9 to 5.9 GHz. The total number of channels D equals 100, and the effective bandwidth W_e is thus 1 GHz.

CSIs from $L = 75$ different locations are measured on the structure within an area of $70\text{cm}\times 20\text{cm}$. The measurement resolution is 5cm, i.e., the distance between two adjacent locations is 5cm. For each of the 75 locations, we formulate $M = 5$ location fingerprints.

B. Metrics for Performance Evaluation

We consider the CSIs collected in the experiment as input to the fingerprint generation procedure in the online phase,

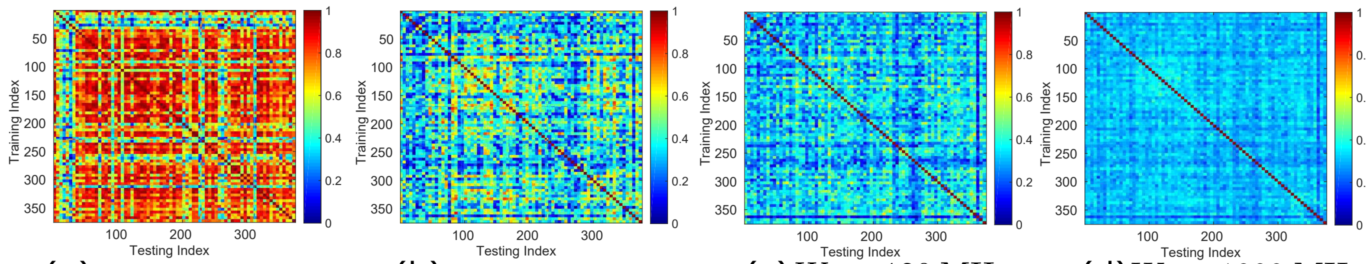

(a) $W_e = 10$ MHz (b) $W_e = 40$ MHz (c) $W_e = 120$ MHz (d) $W_e = 1000$ MHz

Fig. 6. Resonating strength matrix under different W_e.

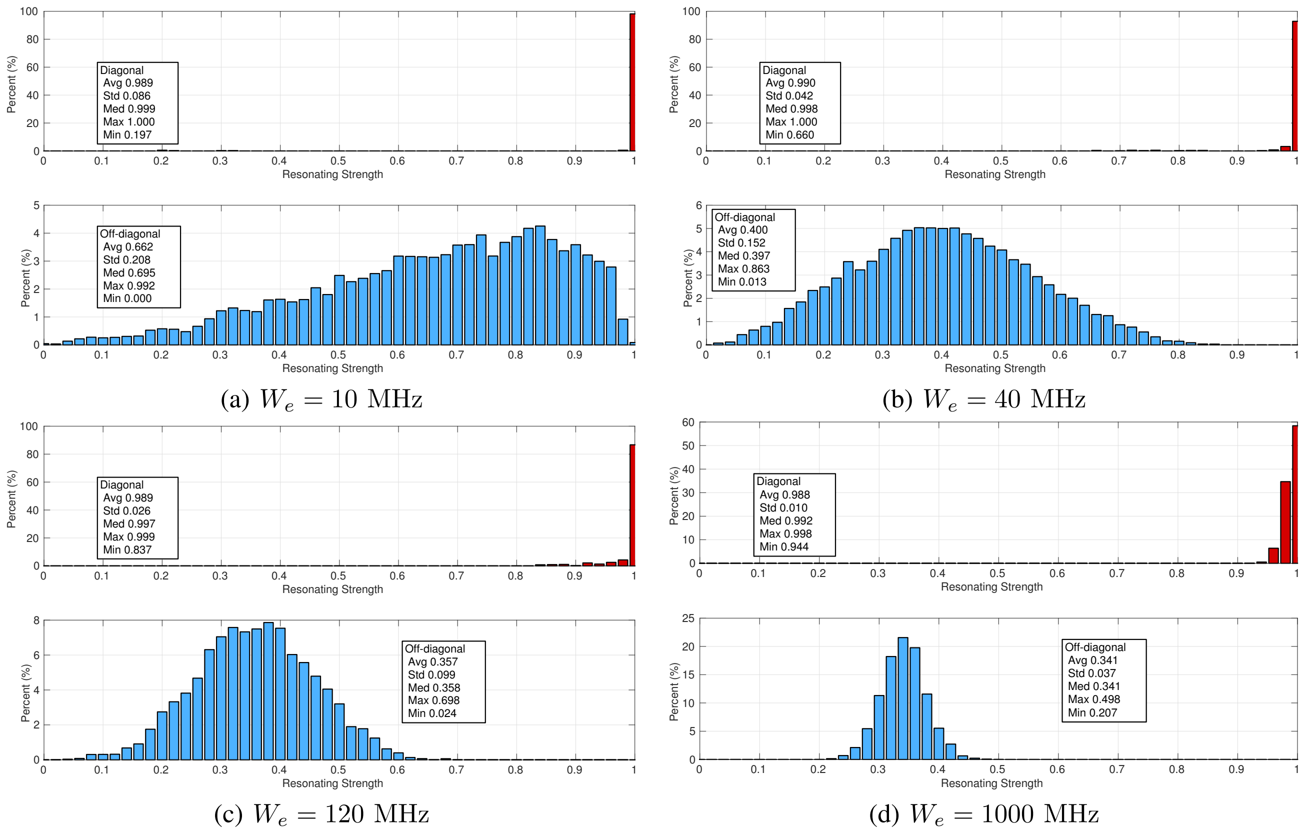

Fig. 7. Histogram of diagonal and off-diagonal entries under different W_e.

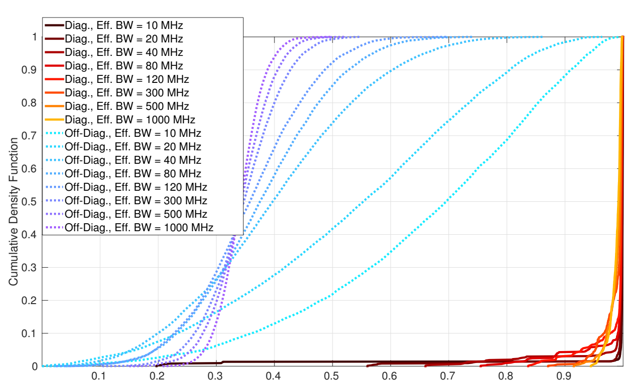

Fig. 8. Cumulative density functions of diagonal and off-diagonal entries of the resonating strength matrix under different W_e.

and store all CSIs into the fingerprint database. For evaluation purpose, we assume that the same CSIs are obtained in the offline phase. Denote the m-th location fingerprint formulated at location ℓ as $\mathbf{G}_m[\ell]$, we calculate the resonating strength matrix $\mathbb{R}$ with the (i,j)-th entry of $\mathbb{R}$ given by $\gamma[\mathbf{G}_m[\ell], \mathbf{G}_n[\ell']]$, where $m = \text{Mod}(i, M)+1$, $\ell = \frac{i-m-1}{M}+1$, $n = \text{Mod}(j, M)+1$, and $\ell' = \frac{j-n-1}{M}+1$. Here, Mod is the modulus operator. Notice that, $[\mathbb{R}]_{i,j} = 1$ if $i = j$. Here, i is termed as the training index, while j is termed as the testing index.

We define the entries of $\mathbb{R}$ calculated from CSIs obtained at the same locations as the *diagonal entries*, while those calculated using CSIs obtained from different locations as the *off-diagonal entries*. We demonstrate the histograms and cumulative density functions for the diagonal and off-diagonal entries.

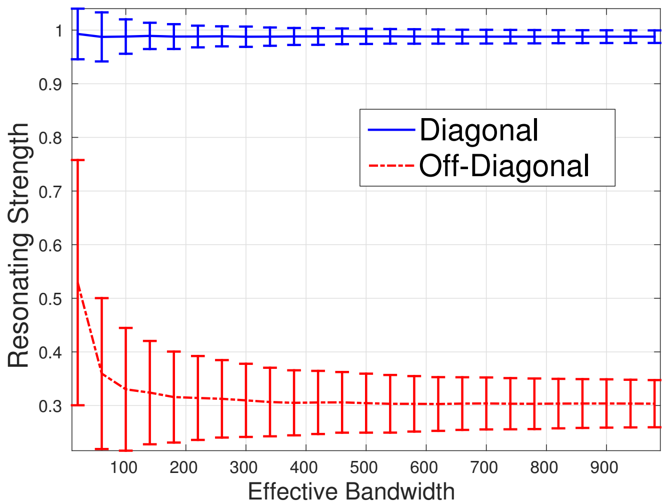

Fig. 9. Mean and standard deviation of the diagonal and off-diagonal entries of the resonating strength matrix under different W_e.

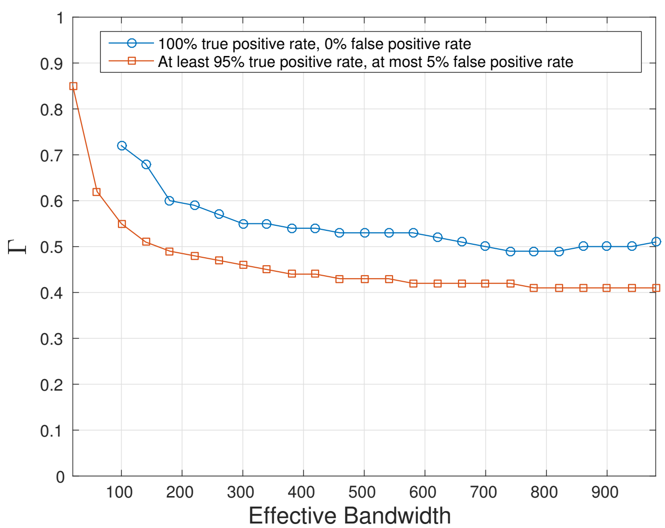

Fig. 10. Threshold Γ under different W_e to achieve (i) $P_{\mathsf{TP}} = 100\%$ and $P_{\mathsf{FP}} = 0\%$ (ii) $P_{\mathsf{TP}} \geq 95\%$ and $P_{\mathsf{FP}} \leq 5\%$.

Based on $\mathbb{R}$, we evaluate the localization performances using the metrics of the true positive rate, denoted as P_{TP}, and the false positive rate, denoted as P_{FP}. P_{TP} is defined as the probability that the IPS localizes the device to its correct location, while P_{FP} captures the probability that the IPS localizes the device to a wrong location, or fails to localize the device.

In the performance evaluation, the CSI sifting parameter τ is set as 0.8.

C. Performance Evaluation

Resonating Strength Matrix under Different W_e
Fig. 6 demonstrates $\mathbb{R}$ with $W_e \in [10, 40, 120, 1000]$ MHz. We observe that when $W_e = 10$ MHz, there exists many large off-diagonal entries in $\mathbb{R}$, indicating severe ambiguities among different locations. When the total bandwidth W_e increases, the ambiguities among different locations are significantly eliminated, while the resonating strengths within the same location are almost unchanged.

Distribution of Diagonal and Off-diagonal Entries under Different W_e
Fig. 7 visualizes the distribution of the diagonal and off-diagonal entries of $\mathbb{R}$ with different $W_e \in [10, 40, 120, 1000]$ MHz using histograms. Statistics of the diagonal and off-diagonal entries are shown as well. As we can see, the resonating strengths at the same location are identical with different W_e, implying high stationarity of the proposed IPS. On the other hand, the off-diagonal entries are more suppressed and approaches a Gaussian-like distribution when W_e increases. We also observe an enlarged gap between the diagonal and off-diagonal entries when W_e increases, indicating a better separability among different locations. The increase of W_e also reduces the variations of diagonal and off-diagonal entries, as shown by the decreasing standard deviations. Moreover, a large W_e removes the outliers in the diagonal entries: when $W_e = 10$ MHz, the minimum value of diagonal entries is 0.197, while the minimum value increases to 0.944 when $W_e = 1000$ MHz. Thus, a large W_e improves the robustness of the IPS against outliers.

Cumulative Density Functions of Diagonal and Off-diagonal Entries under Different W_e
In Fig. 8, we demonstrate the cumulative density functions of diagonal and off-diagonal entries with $W_e \in [10, 20, 40, 80, 120, 300, 500, 1000]$ MHz. As can be seen from the figure, a large W_e reduces the spread of both the diagonal and off-diagonal entries, which agrees with the results shown in Fig. 7.

Mean and Standard Deviation Performances under Different W_e
Fig. 9 depicts the impact of W_e on the mean and standard deviation performances for both diagonal and off-diagonal entries. The upper and lower bars indicate the $\pm\sigma$ bounds with respect to the average, where σ stands for the standard deviation. We conclude that: a large W_e improves the distinction among different locations, but also reduces the variation of resonating strengths at the same locations as well as among different locations. In other words, a large W_e makes the IPS performance more stable and predictable.

Threshold Γ Settings under Different W_e
Fig. 10 depicts the smallest threshold Γ under $W_e = [20, 60, 100, \cdots, 1000]$ MHz to achieve (i) $P_{\mathsf{TP}} = 100\%$ and $P_{\mathsf{FP}} = 0\%$ (ii) $P_{\mathsf{TP}} \geq 95\%$ and $P_{\mathsf{FP}} \leq 5\%$. We observe a decreasing in Γ when W_e is larger, which can be justified by the fact that the gap between the diagonal and off-diagonal entries enlarges when W_e becomes larger. When $W_e = 20$ MHz, the IPS fails to achieve $P_{\mathsf{TP}} = 100\%$ and $P_{\mathsf{FP}} = 0\%$. Fig. 10 also implies that we can achieve a perfect 5cm localization if Γ is chosen appropriately.

D. Discussion of Experiment Results

Based on the experiment results, we conclude that a large W_e is imperative for the robustness, stability, and performance of the proposed IPS. By formulating the location fingerprint that concatenates multiple channels, the proposed IPS achieves

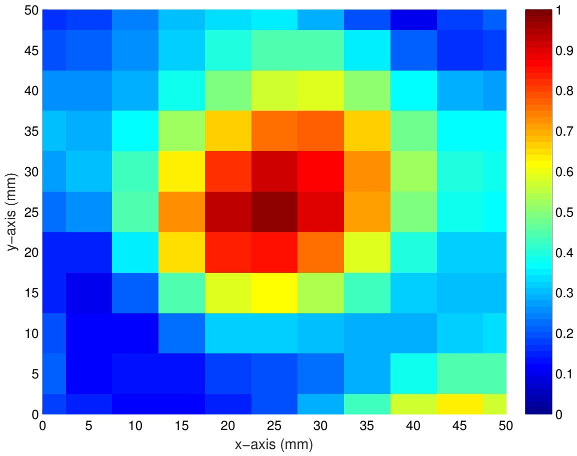

Fig. 11. TR resonating strength near the intended location with a measurement resolution of 0.5cm.

a perfect centimeter localization accuracy in a NLOS environment with one pair of single-antenna WiFi devices.

Notice that the localization accuracy is limited by the 5cm resolution of the measurement structure. In an additional experiment, we refine the measurement resolution to 0.5cm. The TR resonating strengths near the intended location is shown in Fig. 11 with $W_e = 125$ MHz, which demonstrate that the localization accuracy can reach $1 \sim 2$cm in an NLOS environment.

V. Conclusion

In this paper, we present a WiFi-based IPS that exploits the frequency diversity to achieve centimeter accuracy for indoor localization. The proposed IPS fully harnesses the frequency diversity by CSI measurements on multiple channels via frequency hopping. Impacts of synchronization errors and interference are mitigated by CSI sanitization, sifting, and averaging. The averaged CSIs of different channels are then concatenated together into location fingerprints to augment the effective bandwidth. The location fingerprints are stored into a database in the offline phase, and are used to calculate the TR resonating strength in the online phase. Finally, the proposed IPS determines the location based on the resonating strengths. Extensive experiment results of measurements on a 1 GHz frequency band demonstrate the centimeter localization accuracy of the proposed IPS in a typical office environment with a large effective bandwidth.

References

[1] J. G. McNeff, "The global positioning system," *IEEE Transactions on Microwave Theory and Techniques*, vol. 50, pp. 645–652, Mar 2002.

[2] E. Bruns, B. Brombach, T. Zeidler, and O. Bimber, "Enabling mobile phones to support large-scale museum guidance," *IEEE MultiMedia*, vol. 14, pp. 16–25, April 2007.

[3] S. Wang, S. Fidler, and R. Urtasun, "Lost shopping! monocular localization in large indoor spaces," in *Proceedings of the IEEE International Conference on Computer Vision*, pp. 2695–2703, 2015.

[4] Z. Yang, Z. Zhou, and Y. Liu, "From RSSI to CSI: Indoor localization via channel response," *ACM Computing Surveys (CSUR)*, vol. 46, no. 2, pp. 25–1, 2013.

[5] J. Hightower, R. Want, and G. Borriello, "SpotON: An indoor 3D location sensing technology based on RF signal strength," UW CSE 00-02-02, University of Washington, Department of Computer Science and Engineering, Seattle, WA, February 2000.

[6] L. Ni, Y. Liu, Y. C. Lau, and A. Patil, "LANDMARC: indoor location sensing using active RFID," in *Pervasive Computing and Communications, 2003. (PerCom 2003). Proceedings of the First IEEE International Conference on*, pp. 407–415, March 2003.

[7] Q. Zhang, C. H. Foh, B. C. Seet, and A. C. M. Fong, "Rss ranging based wi-fi localization for unknown path loss exponent," in *Global Telecommunications Conference (GLOBECOM 2011), 2011 IEEE*, pp. 1–5, Dec 2011.

[8] B. Campbell, P. Dutta, B. Kempke, Y.-S. Kuo, and P. Pannuto, "Decawave: Exploring state of the art commercial localization," *Ann Arbor*, vol. 1001, p. 48109.

[9] P. Steggles and S. Gschwind, *The Ubisense smart space platform*. na, 2005.

[10] P. Bahl and V. Padmanabhan, "RADAR: an in-building RF-based user location and tracking system," in *Proc. IEEE INFOCOM*, vol. 2, pp. 775–784 vol.2, 2000.

[11] M. Youssef and A. Agrawala, "The Horus WLAN location determination system," in *Proceedings of the 3rd International Conference on Mobile Systems, Applications, and Services*, MobiSys '05, (New York, NY, USA), pp. 205–218, ACM, 2005.

[12] P. Prasithsangaree, P. Krishnamurthy, and P. Chrysanthis, "On indoor position location with wireless LANs," in *Personal, Indoor and Mobile Radio Communications, 2002. The 13th IEEE International Symposium on*, vol. 2, pp. 720–724 vol.2, Sept 2002.

[13] S. Sen, B. Radunovic, R. R. Choudhury, and T. Minka, "You are facing the Mona Lisa: Spot localization using PHY layer information," in *Proceedings of the 10th International Conference on Mobile Systems, Applications, and Services*, MobiSys '12, (New York, NY, USA), pp. 183–196, ACM, 2012.

[14] J. Xiao, W. K.S., Y. Yi, and L. Ni, "FIFS: Fine-grained indoor fingerprinting system," in *Computer Communications and Networks (ICCCN), 2012 21st International Conference on*, pp. 1–7, July 2012.

[15] Y. Chapre, A. Ignjatovic, A. Seneviratne, and S. Jha, "CSI-MIMO: Indoor Wi-Fi fingerprinting system," in *Local Computer Networks (LCN), 2014 IEEE 39th Conference on*, pp. 202–209, Sept 2014.

[16] Z. Wu, Y. Han, Y. Chen, and K. R. Liu, "A time-reversal paradigm for indoor positioning system," *IEEE Trans. Veh. Commun.*, vol. 64, pp. 1331–1339, April 2015.

[17] C. Chen, Y. Chen, H. Q. Lai, Y. Han, and K. J. R. Liu, "High accuracy indoor localization: A WiFi-based approach," in *2016 IEEE International Conference on Acoustics, Speech and Signal Processing (ICASSP)*, pp. 6245–6249, March 2016.

[18] B. Wang, Y. Wu, F. Han, Y. Yang, and K. R. Liu, "Green wireless communications: A time-reversal paradigm," *IEEE J. Select. Areas Commun.*, vol. 29, pp. 1698–1710, September 2011.

[19] M. Fink, "Acoustic time-reversal mirrors," in *Imaging of Complex Media with Acoustic and Seismic Waves* (M. Fink, W. Kuperman, J.-P. Montagner, and A. Tourin, eds.), vol. 84 of *Topics in Applied Physics*, Springer Berlin Heidelberg, 2002.

[20] M. Fink, C. Prada, F. Wu, and D. Cassereau, "Self focusing in inhomogeneous media with time reversal acoustic mirrors," in *Ultrasonics Symposium, 1989. Proceedings., IEEE 1989*, pp. 681–686 vol.2, Oct 1989.

[21] C. Dorme, M. Fink, and C. Prada, "Focusing in transmit-receive mode through inhomogeneous media: The matched filter approach," in *Ultrasonics Symposium, 1992. Proceedings., IEEE 1992*, pp. 629–634 vol.1, Oct 1992.

[22] F. Han, Y.-H. Yang, B. Wang, Y. Wu, and K. J. R. Liu, "Time-reversal division multiple access over multi-path channels," *IEEE Trans. Commun.*, vol. 60, pp. 1953–1965, July 2012.

[23] J. Heiskala and J. Terry, Ph.D., *OFDM Wireless LANs: A Theoretical and Practical Guide*. Indianapolis, IN, USA: Sams, 2001.

[24] J. J. van de Beek, O. Edfors, M. Sandell, S. K. Wilson, and P. O. Borjesson, "On channel estimation in ofdm systems," in *Vehicular Technology Conference, 1995 IEEE 45th*, vol. 2, pp. 815–819 vol.2, Jul 1995.

[25] T.-D. Chiueh and P.-Y. Tsai, *OFDM Baseband Receiver Design for Wireless Communications*. John Wiley and Sons (Asia) Pte Ltd, 2007.

[26] M. Speth, S. Fechtel, G. Fock, and H. Meyr, "Optimum receiver design for wireless broad-band systems using OFDM—Part I," *IEEE Trans. Commun.*, vol. 47, pp. 1668 –1677, nov 1999.

[27] A. V. Oppenheim, R. W. Schafer, and J. R. Buck, *Discrete-time Signal Processing (2nd Ed.)*. Upper Saddle River, NJ, USA: Prentice-Hall, Inc., 1999.

[28] M. Speth, S. Fechtel, G. Fock, and H. Meyr, "Optimum receiver design for OFDM-based broadband transmission II: A case study," *IEEE Trans. Commun.*, vol. 49, pp. 571 –578, apr 2001.

[29] "Ettus Research LLC." http://www.ettus.com/.